Detection of Retinal AVR and CDR Using Active Contours with Blind Deconvolution and CLAHE Fusion (Active-BDCLF)

Niladri Halder[1], Dibyendu Roy[2], Rajib Banerjee[3], Pulakesh Roy[2], Sankar Narayan Patra[1] and Subhankar Bandyopadhyay[1]

[1]Instrumentation & Electronics Engineering, Jadavpur University, West Bengal, India
[2]University Institute of Technology, the University of Burdwan, West Bengal, India
[3]School of Computer Science (SoCS), University of Petroleum and Energy studies (UPES), Dehradun, India

Corresponding Author: **Rajib Banerjee**

Abstract: Various retinal disorders, commonly diabetic and hypertensive retinopathy, can damage the optic nerve, potentially leading to permanent vision loss. Clinical observations often detect these conditions, such as abnormalities in retinal blood vessel diameter and the optic cup-to-disc ratio. High blood pressure can cause retinal vessel thinning and optic cup dilation, disrupting the normal arterio-venous ratio (AVR) and cup-to-disc ratio (CDR). This disruption may result in nerve fiber damage, hemorrhages, and cotton wool spots. This study proposes an automated retinal optic disk and vessel segmentation from pre-processed retinal images. The segmentation was done using a ring mask created by superimposing two circles with the optic disk center and radii of 3D/2 and 1.5D/2, where D denotes the diameter of the optic disk. The maximum AV crossing was avoided within the retinal mask to simplify the process. Validations were performed by comparing the results with a predefined manually segmented dataset, achieving accuracies of 98.6% and 97.8% for retinal optic disk and optic cup, respectively, and 98.73% for retinal vessels. This algorithm could aid ophthalmologists in identifying retinal disorders accurately and automatically.

Keywords: Active Contour, Contrast Limited Adaptive Histogram Equalization, Blind Deconvolution, Region-based classification, Cup Disc Ratio, Artery Vein Ratio

1. Introduction

Glaucoma, considered one of the major reasons for blindness, results in an estimated 12% of total blindness cases and is anticipated to affect almost 11 million people with bilateral blindness. The most common type of glaucoma globally is Primary Open-Angle

Glaucoma (POAG), which impacts 74% of individuals diagnosed with the condition. Based on stratified estimates derived from population studies, it is expected that almost 11.2 million people in India, accounting for nearly 4.6% of the people over the age of 40, are affected by glaucoma [4]. Detecting and treating this disease, which can potentially lead to blindness, presents significant challenges since the majority of those affected remain undiagnosed.

Hypertension can narrow the vessels inside the eye, reducing blood flow to the optical nerve and potentially resulting in blindness. Likewise, elevated pressure within the eye in cases of glaucoma can harm the optic nerves and affect vision. Research has suggested that individuals with hypertension may be at an increased likelihood of developing open-angle glaucoma, a group of eye conditions that damage the optic nerve. The possibility of this risk seems to surge among people with severe or poorly managed hypertension over a prolonged period.

Unfortunately, most associated instances do not exhibit symptoms, although they can be detected using retinal Fundus imaging. Appropriate diagnosis and managing the disease in a clinical setting require careful valuation of variations in the optical nerve head (ONH), measurement of intraocular pressure (IOP), and identification of defects in the visual field. Diagnosing typical ONH alterations in the donor's eyes may be more difficult to assess because of the optic disk's pallor and swelling. Additionally, early vascular changes associated with high blood pressure can cause a narrowing of the retinal arterioles, changes at the arteriolar junction, such as arteriovenous nicking, and arteriolar light reflexes.[5]. Additionally, vessel bending is acknowledged as a likely cause of hypertension and coronary disorders [6]. It is crucial to measure heart rate, as studies have demonstrated a strong link to an elevated long-term likelihood of stroke [7]. As such, this effort seeks to develop a way to detect probable cases of glaucoma and hypertension in donor eyes by examining the optic disc cupping ratio and micro vascular ratio.

2. CDR Measurement

Fig. 1 provides an organizational chart of the CDR measurement. In the RGB color model, each color composed of 3 primary additive color elements—red, green, and blue—which are represented by the following intensity function:

$$\mathrm{Img}_{\mathrm{RGB}} = [\mathrm{Fn}_{\mathrm{R}}(x,y), \mathrm{Fn}_{\mathrm{G}}(x,y), \mathrm{Fn}_{\mathrm{B}}(x,y)] \quad (1)$$

Where$\mathrm{Fn}_{\mathrm{R}}(x,y)$, $\mathrm{Fn}_{\mathrm{G}}(x,y)$ and $\mathrm{Fn}_{\mathrm{B}}(x,y)$ represent the intensities of the pixel (x,y) in the red, the green, and the blue channels correspondingly. In the standard RGB color space, these are as follows:

$$\text{red} = \begin{pmatrix}0.64\\0.33\end{pmatrix}, \text{green} = \begin{pmatrix}0.30\\0.60\end{pmatrix}, \text{blue} = \begin{pmatrix}0.15\\0.06\end{pmatrix} \quad (2)$$

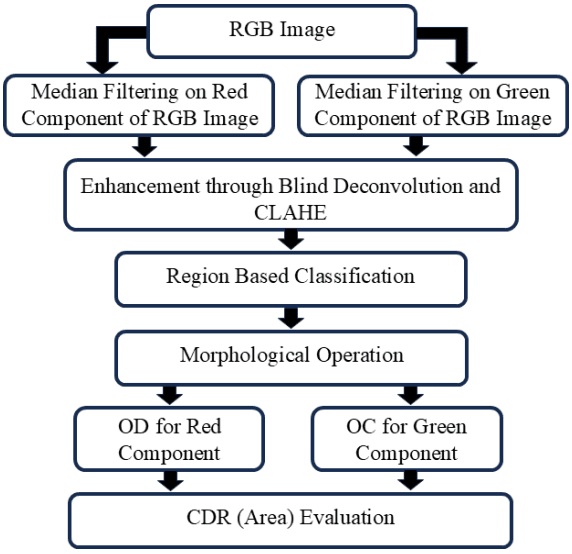

Fig.1: Block diagram explaining the CDR Evaluation

If only brightness information is required, color images may be converted to grayscale images using the proposed transformation equation (3).

$$I_G = 0.333F_R + 0.600F_G + 0.060F_B \quad (3)$$

Here I_G represents the gray equivalent intensity of the RGB image. The red and the green elements of the image Img_{RGB} can be quantified using equation (3). The red and green components of the color image are employed to categorize OD and OC, respectively, as mentioned in Fig. 2.

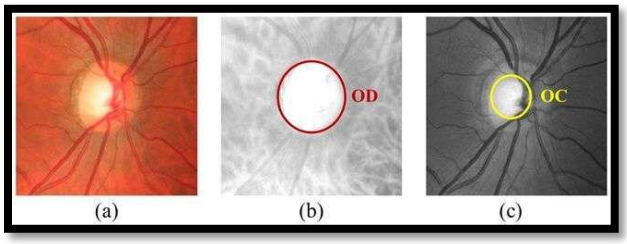

Fig. 2: Random image of HRF dataset represents (a) cropped OD and OC, (b) red channel marking OD, and (c) green channel marking OC.

The advanced technique of CLAHE has been employed to reduce noise through median filtration and enhance the image. Secondly, the use of the regional classification made it possible to detect OD and OC. The operations based on morphology such as dilation, erosion, opening, and closing are used to isolate the OD and OC features.

3. AVR Measurement

The vessel's segmentation and AVR calculation have been made in two steps mentioned in Fig. 3(a) and Fig. 3(b). In the first step, vessels of the overall RGB retinal image have

been segmented by fusioning Blind Deconvolution and advanced CLAHE technique followed by Active Contour-based vessel segmentation skills. In the second step, firstly the optic disk (OD) and its average diameter (D) and then the overlapping area between$\pi(3D/2)^2$ and $\pi(1.5D/2)^2$ has been measured.

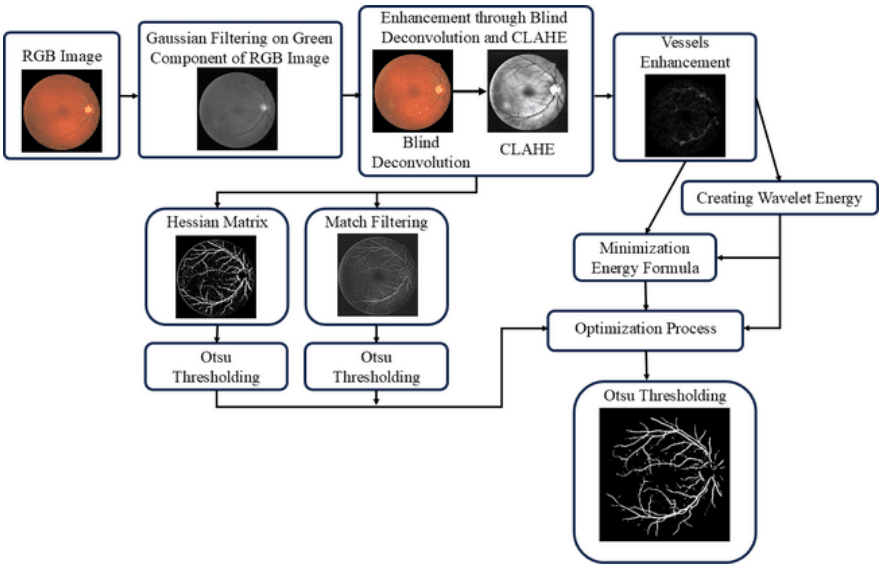

Fig. 3a: Block diagram representing vessels Detection

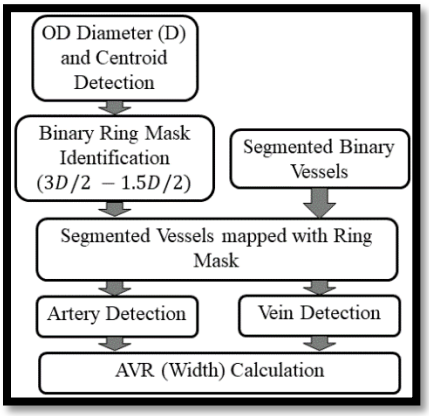

Fig. 3b: Block diagram representing AVR Calculation.

Then the segmented vessels within that masked area have been mapped. The reason behind this mask is that within this range the maximum vessels that are mostly affected by hypertension are found and also complexity is reduced. In the final stage of the second step, arteries and veins are separated to measure the area of the artery and vein separately. Arteries and veins are identified using the following parameters [8].

- The color of the arteries is brighter than that of the veins.

- Arteries are generally narrower than the adjacent veins.
- The central reflex (luminous reflex from within the vessels) is more pronounced within the blood arteries and less pronounced in the blood veins.
- Blood vessels typically alternate near the optic disc before branching out.

Fig. 4(a) and fig. 4(b) shows the marking arteries and veins and the proposed region of interest. Finally, AVR concerning the area has been calculated. The measured AVR helps the Ophthalmologist to detect the stages of hypertensive retinopathy.

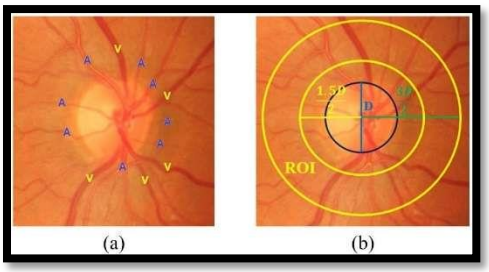

Fig. 4: Random Image cropped from HRF datasets represents (a) marking arteries and veins, and (b) proposed area of interest.

The final step is the validation step where the binary parts of automatic segmented and manual segmented images are considered to identify the true positive and false negative parameters. From here TP, FP, TN, and FN values have been calculated to validate the proposed result set. These steps are depicted in Fig. 5.

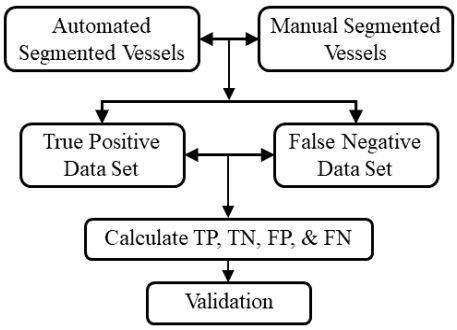

Fig. 5: Functional diagram representing the validation of vessel structure.

Table 1 explains the AVR for normal to accelerated hypertensive retinopathy cases with different risk factors [2] and CDR ranges for normal and affected retina [1].

Table 1: AVR [2]and CDR [1] for different stages of Hypertensive Retinopathy.

Grading of HR	AVR	Indications	Systematic Association	CDR
Normal	0.66-0.75 (Approx.)	Normal	Normal	0.00-0.60 (Approx.)
Grade 1 (Mild)	0.5 (Approx.)	Constricted arterioles, arterial and venous nicking, and thickening of the arteriolar wall.	Loosely linked to cardiovascular disorders	>0.60 (Approx.)
Grade 2 (Moderate)	0.33 (Approx.)	Hemorrhages, along with both hard and soft exudates.	Heart attacks, strokes, and even deaths from cardiovascular diseases.	>0.60 (Approx.)
Grade 3 (Combined)	0.25 (Approx.)	Hemorrhages, along with both hard and soft exudates.	Heart attacks, strokes, and even deaths from cardiovascular diseases.	>0.60 (Approx.)
Grade 4 (Accelerated HR)	Fine Cords <0.2 (Approx.)	Swelling of the optic disc and loss of vision.	Kidney failure and death	>0.60 (Approx.)

4. Literature Review:

The retinal vessels are essential for carrying blood from the heart to the retina, and evaluating their caliber can offer valuable information in identifying diseases like hypertension, diabetes, and stroke at an early stage. The AVR and CDR are two frequently used metrics for assessing retinal vessels. This literature review will explore the different techniques employed for calculating AVR and CDR.

The CDR serves as a metric for evaluating the severity of glaucoma by measuring the proportion of the perpendicular depth of the cup relative to that of the optic disc. A greater CDR value is suggestive of a larger optic cup, which has been linked to a heightened risk of glaucoma. Ophthalmologists or optometrists usually calculate the CDR

during a comprehensive eye examination using a specialized device known as a fundus camera to take images of the optic disc. The images are subsequently analyzed to measure the perpendicular dimensions of the ocular cup and the optic nerve head. Some recent studies related to CDR measurement have been mentioned below.

The authors of a study, Al Shalchi, et al. [44], introduced a Grasshopper optimization algorithm as an automated approach for identifying the optic nerve head in retinal images The algorithm is inspired by the social behavior of grasshoppers and is known as the intelligent Grasshopper algorithm. The results highlight the algorithm's exceptional capability and accuracy in detecting the optic disc.

In their study, Buket Toptas and colleagues (Toptas et al., [45]) recommended a method for recognizing the optical disc in retinal fundus images. They accomplished this by applying an optimized color space to the images, which involved converting them from RGB to an innovative color model by applying an artificial bee colony system. The results indicated that in this newly defined color space; the optic disc was more distinctly localized compared to the original RGB color space.

The objective of Mahum R. and colleagues in their study [46] was to utilize deep learning-based feature extraction to detect early-stage glaucoma. They used retinal scan images for training and validation of their proposed model. The first step involved pre-processing the images, followed by segmenting and selecting the focused region. Next, the hybrid feature descriptors were used to extract the features of the optic disc (OD) from images that include the optical cup region.

A new technique for detecting glaucoma called Densenet-77-based Mask-RCNN has been introduced by Nazir T. and colleagues in their study [47]. To address the challenges associated with glaucoma detection, they initially applied data augmentation and added blurriness to samples to increase data diversity. Ground-truth (GT) images were then used to generate annotations, and The Densenet-77 framework was leveraged for feature extraction at the Mask-RCNN stage to calculate deep key features. Finally, the customized Mask-RCNN model used the calculated structures to identify and segment the OD and OC.

An improved version of the Harris corner location algorithm was suggested by Deng L., et al. [48]. The proposed algorithm takes into account the thick vessels and prominent gray variations in the retinal photograph, with the optic disc area containing the highest number of corners. The main approach includes extracting the region of interest using a matching filter, followed by vascular detection, image optimization, and additional methods. The Harris corner detection algorithm is subsequently enhanced using similarity to identify the corner of the region of interest.

Vascular segmentation is a key component of medical image analysis that has been extensively researched in academic work. This document offers a concise review of some commonly employed methods to segment the retinal vessel's structure.

In their study, Rehman A. et al. [49] propose a trained method for extracting retinal blood vessels. The algorithm comprises two refinement stages that perform filtering and relative histogram analysis following image refinement and quality improvement. Data attributes, including vessel monitoring, peak curvature, and wavelet coefficients, are subsequently retrieved for each pixel. These attributes are then separated through a support vector machine and the k-nearest neighbors'.

In their study, Arsalan M and colleagues [50] present two innovative shallow deep learning models, referred to as DSF-Net and DSA-Net that can effectively identify retinal vasculature. The authors utilize semantic segmentation to analyze raw color fundus images and screen for diabetic and hypertensive retinopathies with high precision.

In their work, Pal M and colleagues [51] suggest an automated technique for segmenting the retinal vasculature. This technique utilizes a Gabor filter bank that has been optimized using a lattice search across the entire constraint space. Additionally, the author employed a novel strip-wise classification method and also incorporated Tophat attributes and ridge data, based on the Eigenvalue spectrum of the Hessian matrix, to improve the accuracy of vessel capture, in addition to the optimized Gabor features.

Boudegga H et al. [52] introduce an innovative DL method for retinal vessel structure segmentation in their study. The key innovation of their work lies in the suggestion of a U-shaped deep learning model that uses efficient convolution layers to improve segmentation accuracy while minimizing computational complexity. Additionally, the authors currently use Data preparation and enhancement methods tailored to the characteristics of retinal images and blood vessels, which constitutes their second major contribution.

In their study, Ooi A et al. [53] recommend a way for segmenting vessel structure from retinal images employing interactive methods grounded in Canny edge detection. The pre-processing phase involves removing the green components, CLAHE, and removing the retinal skeleton. Subsequently, the Canny algorithm-based edge recognition techniques is employed.

The literature review highlights the effectiveness and promise of the image-processing methods examined in these studies for measuring significant parameters like the AVR and CDR. However, it is crucial to recognize that there are still specific constraints and opportunities for improvement.

Some retinal image processing techniques are sensitive to image quality factors such as low resolution, noise, uneven illumination, and motion artifacts. In real-world clinical

settings, where image quality may vary, these techniques may yield suboptimal results or require pre-processing steps.

Certain retinal image processing techniques may be computationally demanding, requiring substantial computational resources or long processing times. This can limit their practical application in real-time or resource-constrained environments.

Obtaining accurate and comprehensive ground truth annotations for retinal images can be challenging and time-consuming. This limitation can affect the expansion and evaluation of image-processing algorithms, making it difficult to establish their true efficacy.

The processing algorithm lacks compact techniques that can effectively handle multiple target features, such as optic disks, retinal vessels, hemorrhages, and others.

5. Motivation and Contribution

Motivation:

Due to the potential cases of diabetes, glaucoma, and hypertension, examination of the CDR and AVR is an imperative aspect. One possible approach for the early detection of these diseases is retinal image analysis. Retinal image processing is fueled by the desire to improve diagnostic precision and gain valuable knowledge about different eye conditions and diseases. Retinal image analysis focuses on analyzing and obtaining meaningful data derived from retinal scans, such as identifying key features like the optic disc, retinal vessels, and hemorrhages, along with detecting abnormalities and signs of eye diseases. The motivation lies in the enhancement of the early detection, monitoring, and treatment of eye disorders, thereby improving patient outcomes and overall eye health.

Contribution:

The contribution to developing the proposed retinal AVR and CDR detection involves several key aspects.

- The contribution encompasses the utilization of multiple algorithms for tasks such as enhancing, segmenting, extracting features, and classifying to derive significant and valuable information from the retinal images.
- We need to gather a comprehensive and heterogeneous dataset of retinal images to support the development and evaluation of the Active-BDCLF algorithm. Our role is to compile and tag these datasets to verify they comprehensively represent retinal conditions and their variations.
- Lastly, the developed algorithms are refined and enhanced through comprehensive testing, thorough evaluation, and meticulous validation. This includes comparing the

algorithms to existing ones, evaluating performance metrics like accuracy, sensitivity, and specificity, and performing Clinical trials to validate their efficacy and dependability in practical settings. The development of algorithms for retinal image processing involves designing algorithms, curating datasets, fostering interdisciplinary collaboration, and conducting rigorous evaluations, all to enhance the precision and medical relevance of retinal image evaluation.

6. Dataset:

The Active-BDCLF algorithm was estimated by freely accessible datasets like DRIVE, HRF, STARE, CHASEDB1, INSPIRE-AVR, and others to develop a fully automated monitoring system.

The DRIVE dataset was created as part of a diabetic testing campaign in The Netherlands. The trial involved 400 diabetic individuals ranging in age from 25 to 90 years. Out of this collection, 40 images were selected at random: 33 exhibiting no signs of diabetic retinopathy and 7 showing early-stage, mild diabetic retinopathy. These visuals were obtained with a Canon CR5 non-mydriatic 3CCD camera featuring a 45-degree field of view (FOV). Each image was confirmed at a resolution of 768 × 584 pixels, using an 8-bit color model, with a circular field of view covering approximately 540 pixels. The photos were reaped around the FOV, and every photo was accompanied by a 'mask' delineating the FOV.

The collection of 40 images was divided into a training set and a test set, each containing 20 images. The training collection comprises a solitary manual segmentation of the vascular structure. In relation to the test set, two manual delineations are included: one acts as the standard, and the other facilitates a comparison between the computer-generated segmentation and an independent human observer. Each retinal image also comes with a mask defining the region of interest. The human observers responsible for manual segmentations were trained by an experienced ophthalmologist and instructed to label pixels as vessels only if they were at least 70% confident in their assessment.

The INSPIRE-AVR dataset is publicly available and consists of 40 annotated retinal images with significant vascular abnormalities, optic disc region, and artery-vein ratio. It is specifically used for classifying and grading various hypertension-related complications. The annotations were made by two specialists using a hybrid automated tool developed by the University of Wisconsin, Madison, WI, USA [32].

The HRF imaging dataset, created by a collaborative research group, is designed to aid in the formulation of clinical decision-support tools for diagnosing different retinal irregularities. It covers 45 retinal images from participants, with 15 from healthy

individuals, 15 from glaucomatous cases, and 15 from diabetic retinopathy (DR) cases [33]. These pictures are recorded at 3504 × 2336 pixels resolution, 24 bits per pixel, utilizing a CANON CF-60 UVI camera with a 60-degree viewing angle.

The STARE dataset comprises approximately 400 images, with 50 images depicting vascular patterns and 80 featuring Reference standards for optic nerve localization [34]. These pictures were taken at a resolution of 605 × 700 pixels with a 24-bit color depth using a TOPCON TRV-50 fundus camera, offering a 35-degree field of view.

7. Methodology:

The Active-BDCLF can measure the CDR and AVR of an ophthalmoscope image. In the beginning, the Active-BDCLF approach utilizes median filtering and Gaussian filtering. Subsequently, the subsections elaborate on the primary contributions, including Blind Deconvolution, CLAHE, and morphological operations.

7.1 Median Filtering:

The median filter is a statistical-based, non-linear approach to signal processing that replaces noisy values in a numerical image or sequence with the median of surrounding values. The outcome of applying the median filter can be determined using equation (4).

$$I_g(x,y) = median\{I_f(x-i, y-j), i,j \in W_{2d}\} \quad (4)$$

Here $I_f(x,y), I_g(x,y)$is the input and the resulting images accordingly, $W_{2d}$is the 2D mask: the size of the mask is $N \times N$ where N is commonly odd such as $3 \times 3, 5 \times 5$etc.

The mathematical analysis of a non-linear median filter is comparatively complicated for randomized noise images. For the image where the average noise is zero in a normal distribution, the median filter noise variance is approximate.

$$\sigma_{mid} = \frac{1}{4nf^2(\bar{n})} \approx \frac{\sigma_i^2}{n+\frac{\pi}{2}-1} \cdot \frac{\pi}{2} \quad (5)$$

Where $\sigma_i^2$the power of noise, the variance, is $N$is the size of the mask of the filter, $f^2(\bar{n})$ is the function representing noise density. The variance of the filtering can be determined using equation (6).

$$\sigma_0^2 = \frac{1}{n}\sigma_i^2 \quad (6)$$

7.2 Gaussian Filtering:

Gaussian filter, a linear class windowed filter, is typically used for image blurring or noise reduction. The unshaped masking that is the edge can be detected simply by subtracting two filtered results from each other. The Gaussian or normal distribution is a probability function that is referred to as a bell function due to its shape. The most common function formula is shown in equation (7).

$$G(x,y) = \frac{1}{2\pi\sigma^2} e^{\{-(x^2+y^2)/2\sigma^2\}} = G(x).G(y) \quad (7)$$

Equation (7) explains that the 2D Gaussian filter is separable. To obtain the Gaussian filtering of the 2D image, the following algorithm is employed.

- Measure the weights of the 1D window, denoted as $G_n^{/}$.
- Process each image line as a one-dimensional signal.
- Process each column of the filtered image as a 1D signal.

Two-dimensional filtering with window $[2n+1] \times [2n+1]$ is condensed to a few one-dimensional filters with a window $[2n+1]$. This signifies a substantial acceleration, particularly for large datasets resulting from the reduction in the number of operators, from O(N²) to O(N).

7.3 Blind Deconvolution

Blind Deconvolution is an approach in image analysis used to improve image quality by fixing image smudges caused by stemming from problems like lens misalignment or imaging system blur. This system assesses both the original image and the blur kernel at the same time, without any previous information about either. Usually, unsupervised Deconvolution modalities operate by repetitively reducing an objective function that calculates the discrepancy between the evaluated deblurred image and the actual blurred image. Unsupervised Deconvolution helps restore images affected by convolution—such as those with motion blur or caused by an image response function—back to their original quality.

The first step in the blind deconvolution algorithm is to estimate the point-spread function (PSF) that causes the visual deterioration. A commonly employed technique for this is the Richardson-Lucy algorithm, which progressively refines the PSF by comparing the degraded image with an estimated version of the restored image. The Richardson-Lucy algorithm is mathematically expressed in equation (8).

$$P_{k+1}(x,y) = P_k(x,y) \frac{\sum_{i,j} \frac{I(x-i,y-j)}{(P_k * I)(x-i,y-j)}}{\sum_{i,j} \frac{P_k(x-i,y-j)}{(P_k * I)(x-i,y-j)}} \quad (8)$$

The appearance includes the projected PSF at repetition k signified asP_k, the tainted image signified as I, and the convolution kernel symbolized by $*$. Primarily, the approach approximations the PSF as P_0 and then constantly upgrades this approximation until merging. The dividend in appearance specifies recovering the degraded image with the estimated PSF, while the divisor specifies the smearing of the revalidated image by the PSF. The procedure apprises the PSF estimation by conveying pixel proximity weights in the tainted image based on their resemblance to the present PSF estimation.

Hessian Blind Deconvolution is an image rebuilding method that concurrently estimates the point-spread function (PSF) and reinstates the image. Below is a high-level process exactness the Hessian Blind Deconvolution process:
Inputs: degraded image I, regularization parameter λ, maximum number of iterations T.
Outputs: estimated PSF P and restored image R.

1. Set the initial values of P and R by randomly assigning values.
2. For t = 1 to T:
    a. Calculate the gradient and Hessian of the cost function concerning P and R.
    b. To obtain the updates ΔP and ΔR for P and R respectively, solve the linear system $H\Delta X = -\nabla f$.
    c. Update P and R using ΔP and ΔRseparately: $P \leftarrow P + \Delta P$ and $R \leftarrow R + \Delta R$.
3. Return P and R as the estimated PSF and restored image, respectively.

Typically, a mixture of an information fidelity period and a regulation period is used as the cost function f in the above algorithm. The data fidelity term evaluates the degree of resemblance between the estimated image and the observed degraded image. In contrast, the regularization term discourages solutions that lack smoothness or do not meet other desired criteria.
To approximate the point-spread function (PSF) and the restored image simultaneously using the Hessian Blind Deconvolution algorithm, the Hessian matrix is calculated as the 2nd-order derivative of the cost function. Are iterative method, such as conjugate gradient, is then used to resolve the linear system HΔX = -∇f. The regularization parameter λ is used to balance the trade-off between data fidelity and regulation, while the iteration ceiling T sets the number of times the process will run before returning the estimated PSF and restored image. The improvement of the retinal dataset using proposed blind Deconvolution is illustrated in Fig. (6).

7.4 Modified CLAHE

Histogram equalization enhances the contrast ratio by redistributing the brightness levels across the frequency distribution. In this research, CLAHE, with specific adjustments, was applied to strengthen retinal grayscale images. Initially, the contrast of the grayscale image was enhanced using the formula outlined in the equation (9).

$$Im(x,y) = \frac{fn(x,y) - fn(min)}{fn(max) - fn(min)} * 2^{bpp} \quad (9)$$

Here $Im(x,y)$signifies the input data,$fn(x,y)$, $fn(min)$, and $fn(max)$represent the pixel intensity values, and the least and greatest pixel intensities, respectively. The generated contrast-adjusted image is subsequently used as the input for CLAHE. In CLAHE, the source image is divided into non-overlapping contextual areas, or tiles, each with its local histogram. Before determining the total probability distribution, and amplifying contrast

intensity, the histogram of each segment is truncated using a user-defined clipping threshold. The clipping threshold corresponds to a multiple of the average histogram peak within the surrounding region, as shown in equation (10).

$$[Hist\_Hight]_{Avg} = \frac{[Pixel(total)]_{contextual}}{[Pixel(total)]_{gray}} \quad (10)$$

For contextual scale say $M \times N$ and Pbe the number of histogram bins, the clip limit is assumed by the equation (11).

$$Clip_{Limit} = \begin{cases} 1 & if \quad \frac{\alpha_{cf} MN}{[P_n]_{hist}} < 1 \quad for \quad 0 < \alpha \leq 1 \\ 0 & otherwise \end{cases} \quad (11)$$

In this situation, α_{cf}does the user define a contextual aspect. The precise elevation of the histogram in the contextual area $n_k$is being trimmed using the $Clip_{Limit}$as specified in equation (12) where $[Hist]_k$is the histogram of the specified area.

$$[Hist]_k = \begin{cases} Clip_{Limit} \; if \; n_k = Clip_{Limit} \; for \; k = 1,2, \dots, [P_n]_{hist} - 1 \\ n_k \qquad otherwise \end{cases} \quad (12)$$

Note that,

$$\sum_{k=0}^{[Pn]_{Hist}-1} n_k = MN \quad (13)$$

Total clipped pixels,

$$Clip_{total} = MN - \sum_{k=0}^{[Pn]_{Hist}-1} [Hist]_k \quad (14)$$

By adjusting the histogram again, the area beneath the curve is reestablished to its original range, redistributing the clipped pixel values across the histogram. The reordering can be uniform; however, if not, the clipped pixel standards may be unevenly spread across histogram plots for pixel parameters below the clip limit. The pixels assigned to each histogram bin are determined as described in Equation (15).

$$[Pixel]_{\mu} = \frac{Clip_{total}}{[Pn]_{Hist}} = \frac{MN - \sum_{k=0}^{[Pn]_{Hist}-1} [Hist]_k}{[Pn]Hist} \quad (15)$$

The histogram, once clipped, is being re-scaled by applying equation (16).

$$[Hist]_k = \begin{cases} CLip_{Limit} \quad if \quad n_k + [Pixel]_{\mu} \geq Clip_{Limit} \\ n_k + [Pixel]_{\mu} \qquad otherwise \end{cases} \quad (17)$$

7.5 Morphological Operations:

Morphological filters are derived from various combinations of two primary operations—dilation and erosion—along with a kernel known as a structural component, a bit mask characterized by precise contour and focal point. The structural component's shape determines the filter's impact on the image. Correspondingly, the retinal input image I, the structural component, SE, and the two elementary operators, erosion and dilation, is considered to be in equations (18) and (19).

$$I \ominus SE = \{x \;\; such \; that \quad SE_x \subseteq I\} \quad (18)$$

$$I \oplus SE = \{x \quad such\ that \quad SE_x^s \cap I \neq \Phi\} \tag{19}$$

Where SE_xsignifies the structural componentSE with the standard parameters located in x, while SE_x^ssignifies the symmetric rotation of the structural component located in$x$.

Multiple merged morphological filters can then be distinctly characterized as a mix of the superior components. The basic complex operators are the 'open' and 'close' operators, marked as the erosion-dilation and dilation-erosion operations, respectively, in Equation (20) and Equation (21).

$$I \circledcirc SE = I \ominus SE \oplus SE \tag{20}$$

$$I \odot SE = I \oplus SE \ominus SE \tag{21}$$

The morphological Top-Hatoperation is very effective for individual point marks with all kinds of backgrounds, but it is less useful for tackling the image removal problem with the localized target, that is severely corrupted by noise. It is therefore necessary to supply an improved morphological Top-Hat filter.

The structural component of the innovative Top-Hat filter is designed as follows: design an internal structural element and an external structural element as$SE_0(m \times m)$, complying $SE_i \subset SE_0$. Define Edge Structuring Element as$SE_{Edge} = SE_0 - SE_i$. Thus, the improved Top-Hat operation can be demarcated as in equation (22).

$$Top\_Hat_{I,SE}(x) = \left[\left\{I - \left(I \Theta SE_{Edge}\right) \oplus SE_i\right\}.x\right] \tag{22}$$

7.6 Modified active contour

This method leverages the joint capabilities of the gradient force snake model and the balloon model to detect blood vessels in fundus images effectively. An image-based contour model is a deformable spline curve guided by an internal force that resists deformation, allowing it to move toward objects in the image [59].This behavior is comparable to the way a snake moves through a hollow space. A snake typically avoids the center of a hollow space, instead moving along the walls and corners, constantly searching for openings. Upon finding a hole, it enters, explores, and retreats if the path is blocked. Similarly, when applied to retinal blood vessels, the snake follows the vessel boundaries, where the vessel walls act as the boundaries and the openings or cracks represent potential entry points.

To ensure the snake adheres to the vessel boundaries without deforming them, its energy must remain lower than the internal energy of the vessels. The Gradient Vector Flow (GVF) technique limits the snake's energy [60]. The total energy function of the snake, calculated at a pointv_q, where $q = 0, \ldots, n-1$ is the addition of its inner energy (E_{int}), image energy (E_{img}), and user-defined constraint force E_{Cns}. This relationship is expressed through the equation (23):

$$E_s^* = \int_0^1 E_s(v_q')dq = \int_0^1 [E_{int}(v_q') + E_{img}(v_q') + E_{cns}(v_q')]dq \quad (23)$$

7.6.1 Internal energy of snake:

The stored power of the snake is influenced by the fluidity of the curve E_{smth} and continuity of contourE_{con}.

$$E_{int}^{snake} = E_{con} + E_{smth} \quad (24)$$

Moreover the aforementioned equation can be articulated as in an expanded form as:

$$E_{int}^{snake} = \frac{1}{2}\left(\alpha'(q)|v_q'|^2\right) + \frac{1}{2}\left(\beta'(q)|v_q'|^2\right)$$
$$= \frac{1}{2}\left(\alpha'(q)\left\|\overline{\frac{\partial v'}{\partial q}(q)}\right\|^2 + \beta'(q)\left\|\overline{\frac{\partial^2 v'}{\partial q^2}(q)}\right\|^2\right) \quad (25)$$

To regulate the sensitivity of the snake's length, user-controlled weights $\alpha'(q)$ and $\beta'(q)$are introduced.

7.6.2 Energy of Image:

Consider an image, $Img(m,n)$, with attributes like boundaries, closures, and lines. The vitality of the image can then be expressed as:

$$\ddot{E}_{img} = W_{line}E_{line} + W_{edge}E_{edge} + W_{cls}E_{cls} \quad (26)$$

The proportions of attributes such as line, edge, and closure are displayed by $W_{line}, W_{edge}, W_{cls}$ while their corresponding energies are denoted as $E_{line}, E_{edge}, E_{cls}$. The various energies associated with these features are illustrated below.

Line functional: This refers to the intensity of the image, which can be expressed using the following equation:

$$E_{line} = X(m,n) \quad (27)$$

The scale and sign of W_{line} dictate whether the snake gravitates towards dark or light vessels. In this study, a Gaussian filter is employed on the image to shield the snake from being disturbed by inaccessible noisy pixels. After applying the filter, the equation becomes:

$$E_{line} = Gaussian\_Filter(X(m,n)) \quad (28)$$

Edge function: This parameter is influenced by the gradient of the image

$$E_{edge} = -|\nabla X(m,n)|^2 \quad (29)$$

A snake preliminary beyond the target item may sometimes congregate to a localized noise artifact or minimum. To tackle this problem, a distorting filter is first used and the level of blurriness is gradually reduced to refine the snake-fitting process.

$$E_{edge} = -\left|\ddot{G}_\sigma \times \nabla X(m,n)\right|^2 \quad (30)$$

The term $\ddot{G}_\sigma$refers to a Gaussian blur whereσ represents the standard deviation (SD). The blurry filter can be useful either in the line or the edge function. Given the Marr–Hildreth

philosophy of edge detection, the least values of the function occur at the zero-crossings of $\ddot{G}_\sigma \times \nabla X(m,n)$.

Closure function: To sense the corners and endpoints of the line, the data is blurred using $\ddot{G}_\sigma$. Let $J(m,n)$ represent the image after smoothing.

$$J(m,n) = \ddot{G}_\sigma \times x(m,n) \quad (31)$$

Having gradient angle

$$\hat{\theta} = arctan\left(\frac{J_n}{J_m}\right) \quad (32)$$

The normalized vector pointing along the gradient is

$$\hat{n} = \left(cos\hat{\theta}, sin\hat{\theta}\right) \quad (33)$$

A normalized vector $\hat{n}_\perp$perpendicular to the gradient path

$$\hat{n}_\perp = \left(-sin\hat{\theta}, cos\hat{\theta}\right) \quad (34)$$

The strength of the exit function is specified by

$$E_{cls} = \frac{\partial\hat{\theta}}{\partial\hat{n}_\perp} = \frac{\partial^2 J/\partial^2\hat{n}_\perp}{\partial J/\partial\hat{n}} = \frac{J_{nn}J_m^2 - 2J_{mn}J_mJ_n + J_{mm}+J_n^2}{\left(J_m^2+J_n^2\right)^{3/2}} \quad (35)$$

7.6.3 Constrain Energy:

The accumulated energy managed by the snake's movement, either towards or away from specific objects features typically specified by the user. Using the two energy formulas debated earlier, the snake's concluding energy equation can be derived from equation (36). To prevent the snake from penetrating the vessels and to ensure it follows the wall, the internal energy must be minimized accordingly. Several optimization techniques can be employed for this, such as the gradient descent method [54], discrete approximation methods, and others.

$$\ddot{E}_{img} = W_{line}.Gaussian\_Filter\left(X(m,n)\right) + W_{edge}\left(-\left|\ddot{G}_\sigma \times \nabla X(m,n)\right|^2\right) + W_{cls}\frac{J_{nn}J_m^2 - 2J_{mn}J_mJ_n + J_{mm}+J_n^2}{\left(J_m^2+J_n^2\right)^{3/2}} \quad (36)$$

$$\ddot{E}_{GVF} = \iint \mu\left(\widehat{u_m^2} + \widehat{u_n^2} + \widehat{v_m^2} + \widehat{v_n^2}\right) + \left|\nabla\hat{f}\right|^2\left|\hat{V} - \nabla\hat{f}\right|^2 \partial m\, \partial n \quad (37)$$

The gradient vector flow method is applied in this work to mitigate the external energy exerted on the vessels, which is related to the snake's internal energy.

This GVF model [60] tackles issues such as:

i. Difficulty in achieving convergence when starting from minimum.
ii. Inadequate fusing at concave limits.

The bi-dimensional energy of the GVF vector field is presented in equation (37), where μ represents the tenable smoothing factor. By applying Euler's method to equation (37), the resulting equations are explained:

$$\mu\nabla^2\hat{u} - \left(\hat{u} - \frac{\partial}{\partial m}\widehat{F_{ext}}\right)\left(\frac{\partial}{\partial m}\widehat{F_{ext}}(m,n)^2 + \frac{\partial}{\partial n}\widehat{F_{ext}}(m,n)^2\right) = 0 \quad (38)$$

$$\mu\nabla^2\hat{v} - \left(\hat{v} - \frac{\partial}{\partial n}\widehat{F_{ext}}\right)\left(\frac{\partial}{\partial m}\widehat{F_{ext}}(m,n)^2 + \frac{\partial}{\partial n}\widehat{F_{ext}}(m,n)^2\right) = 0 \quad (39)$$

Solving through iteration with a steady-state value we have

$$\widehat{u_{\iota+1}} = \hat{u}_\iota + \mu\nabla^2\hat{u}_\iota - \left(\hat{u}_\iota - \frac{\partial}{\partial m}\widehat{F_{ext}}\right)\left(\frac{\partial}{\partial m}\hat{F}_{ext}(m,n)^2 + \frac{\partial}{\partial n}\hat{F}_{ext}(m,n)^2\right) \quad (40)$$

$$\widehat{v_{\iota+1}} = \hat{v}_\iota + \mu\nabla^2\hat{v}_\iota - \left(\hat{v}_\iota - \frac{\partial}{\partial n}\widehat{F_{ext}}\right)\left(\frac{\partial}{\partial m}\hat{F}_{ext}(m,n)^2 + \frac{\partial}{\partial n}\hat{F}_{ext}(m,n)^2\right) \quad (41)$$

This result can be substituted with the default external force.

$$F_{ex}^* = \hat{F}_{GVF} \quad (42)$$

7.7 Pseudo code

Below is a sample pseudo code that demonstrates how to perform a Top Hat Transformation on an image by utilizing the opening morphological operation.

1. Algorithm for Blind Deconvoluted CLAHE:

Input: Color retinal image

Output: Colorenhanced image`

Begin

```
blurredImage = imread('blurred_image.jpg');   /* Read the blurred image*/
numIterations = 100; /*Number of iterations for the algorithm*/   /*Set parameters
for blind deconvolution*/
lambda = 0.01; /* Regularization parameter*/
psfSize = [15, 15];  /* Size of the point spread function (PSF) */
psfInitial = fspecial('gaussian', psfSize, 2); /* Initial estimate of PSF */
estimatedImage = deconvblind(blurredImage, psfInitial, numIterations, lambda);
/* Perform blind deconvolution */
    ifsize(estimatedImage, 3) == 3  /* Convert estimatedImage to grayscale if
    needed */
        img = rgb2gray(estimatedImage);
    end
[row, column] = size(img);  /* Calculate the image size */
numBlocksRows = floor(rows / blockSize); /* Divide the image into non-
overlapping blocks */
numBlocksCols = floor(cols / blockSize);
enhancedImg = zeros(rows, cols);  /* Initialize the output enhanced image */
/* Loop through each block */
    fori = 1 :numBlocksRows
        for j = 1 :numBlocksCols
            /* Extract the current block */
```

```
                block = img((i-1)*blockSize+1:i*blockSize, (j-
                1)*blockSize+1:j*blockSize);
                equalizedBlock = histeq(block);  /* Perform histogram
                equalization on the block */
                /* Clip the block's histogram to the specified limit */
                clippedBlock = min(max(equalizedBlock, 0), limit);
                /* Assign the enhanced block to the corresponding region in the
                output image */
                enhancedImg((i-1)*blockSize+1:i*blockSize, (j-
                1)*blockSize+1:j*blockSize) clippedBlock;
            end
        end
        /* Convert the output enhanced image to the original color space if needed */
        If size(estimatedImage, 3) == 3
            enhancedImg = repmat(enhancedImg, [1, 1, 3]);
        end
End
```

2. Algorithm for Morphological operation and TOP-HAT transform

Input: Enhanced gray image

Output: Segmented binary image

```
Begin
    Image(input) =Image(enhanced);   /* Scan the input image */
    /* Employ morphological transformations to clean noise or smooth out the data.*/
    Structuring Element = strel('disk', size);  /* Develop a circular structuring element
    with a specified size*/
    Image(morph) = imopen(Image_gray, SE);  Execute opening function*/
    Image(tophat) = imtophat(Image(morph), SE);  Implement TOP-HAT technique
    for image sharpening*/
    threshold = graythresh(Image(tophat));  /* Implement thresholding to segment the
    target regions in the image*/
    Image_binary = imbinarize(Image(tophat), threshold);
    /*If applicable, apply additional steps to the binary image to achieve more
    precision*/
    /* (e.g., block holes, eliminate small objects) */
End
```

3. Algorithm for Active Contour Model for Vessels Segmentation

Input: Image I, Initial contour C_0, Smoothing parameter μ, Number of iterations N
Output: Final contour C
Begin

1. Initialize the starting contour of the snakeC_0.
2. For each iteration i from 1 to N:
    a. Compute internal forces:
        - Curvature force (based on second derivatives of the contour)
        - Elastic force (based on first derivatives of the contour)
    b. Compute external forces (based on the image gradient or desired edges):
        - Image gradient or edge information (e.g., from a gradient map or energy function)
    c. Combine internal and external forces to compute the new contour:
        - Update contour points by minimizing the energy function:
        $C_{new} = C_{old} + (Force_{internal} + Force_{external})$
    d. Apply smoothing term μ to adjust the contour's smoothness (optional)
    e. If the change in contour position is below a threshold, exit the loop early
3. Return the final contour C

End

7. Result

To assess the performance of the Active-BDCLF, a set of 40 fundus retinal images from the DRIVE database was selected. Of these, 33 images are from healthy patients with no clinical disorders, while 7 images are from patients with clinical abnormalities. For all 40 images, the optic cups, optic discs, and vessel structures were segmented, and measurements for the optic cup diameter, optic disc diameter, and vessel width were obtained using the described automatic process. The Cup-Disc Ratio (CDR) and Artery-Vein Ratio (AVR) were then calculated and compared with the manual data. Fig. 6 illustrates the image enhancement achieved using the advanced CLAHE and Blind Deconvolution fusion techniques.

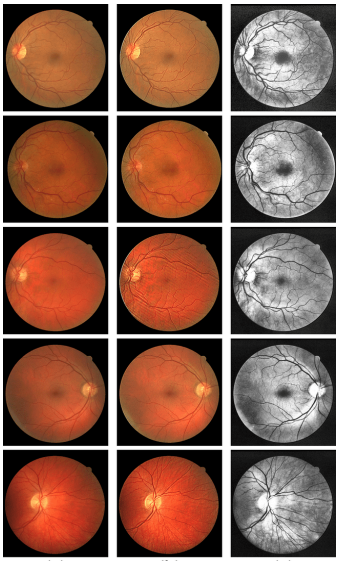

Fig. 6: Result shows the image enhancement techniques using CLAHE and Blind Deconvolution fusion: (a) Input RGB Fundus Image, (b) Enhancement by Blind Deconvolution, and (d) Enhancement by CLAHE after Blind Deconvolution.

Table 2 presents a comparison of the quality measures between images that have been enhanced using CLAHE and the Active-BDCLF techniques. The Active-BDCLF achieves a higher PSNR, indicating superior image quality. Additionally, the proposed technique exhibits a lower MSE than CLAHE, leading to enhanced image fidelity, improved visual quality, and increased accuracy. Furthermore, the higher SSIM measure of the proposed technique compared to CLAHE ensures minimal distortion in the image structure. The results demonstrate that the mentioned technique surpasses CLAHE in terms of image enhancement.

Table 2: Quality measures of PROPOSED and CLAHE

Image	MSE ($Pixel^2$)		PSNR(dB)		SSIM	
	Active-BDCLF	CLAHE	Active-BDCLF	CLAHE	Active-BDCLF	CLAHE
6(a1)	3151.30	4273.50	15.85	11.82	0.4428	0.3390
6(a2)	5316.20	6322.50	16.63	10.12	0.2760	0.1752
6(a3)	3992.91	5161.00	14.89	11.01	0.3379	0.2365
6(a4)	1953.30	2737.30	17.43	13.75	0.6469	0.5456
6(a5)	3162.4	4058.3	18.93	12.05	0.4582	0.3480

Fig. 7 represents the input RGB fundus images of the macula with segmented results of the optic disk and optic cup using the mentioned morphological techniques.

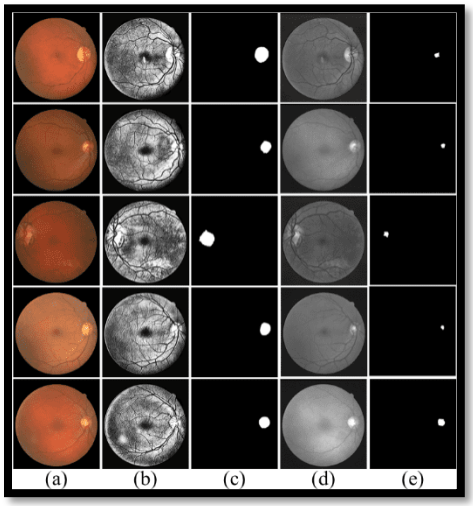

Fig. 7: In this figure, (a) represents the input RGB fundus image, (b), (c), (d) and (e) represent the PROPOSED Enhancement, segmented Optic Disk, green components of the input image, and segmented Optic Cup respectively.

Table 3 provides a comparison between the automatic and manual Cup-to-Disc Ratio (CDR) measurements. The automatic diameter measurements of the Optic Disc (OD) and Optic Cup (OC) in terms of pixels are performed by Active-BDCLF, while the manual diameters are obtained from the specified dataset. The CDR values are computed for both automatic and manual measurements by taking the ratio of their respective areas. The CDR errors are calculated by finding the difference between the manually and automatically determined CDR values.

Table 3: Result shows the comparison of automatic CDR and manual CDR

Sl. No.	$Dia_{OD}(Pixel)$		$Dia_{OC}(Pixel)$		CDR ($Pixel^2$)		$Error_{CDR}$
	Auto	Manual	Auto	Manual	Auto	Manual	
1	230	234	186	190	0.65	0.66	0.01
2	226	224	194	190	0.74	0.72	-0.02
3	218	223	184	186	0.71	0.70	-0.01
4	226	232	178	184	0.62	0.63	0.01
5	228	224	182	178	0.64	0.63	-0.01
6	203	194	179	175	0.78	0.81	0.04
7	216	230	175	178	0.66	0.60	-0.06

8	224	218	184	175	0.67	0.64	-0.03
9	226	225	128	130	0.32	0.33	-0.01
10	224	225	128	125	0.33	0.31	-0.02

The average diameter error for both the optic disc and cup is approximately ±4%. Graphs depicting the correlation between the automatically detected diameter and manually measured diameter for the optic disc and cup can be observed in Fig. 8a and Fig. 8b respectively.

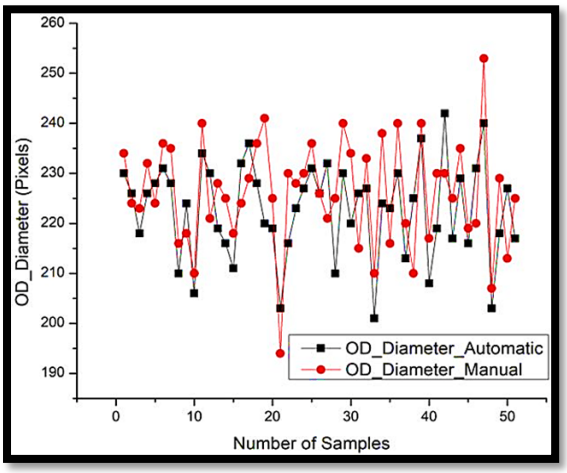

Fig. 8a: This figure represents the comparison of the diameter of the Optic Disk segmented by using manual and automated processes.

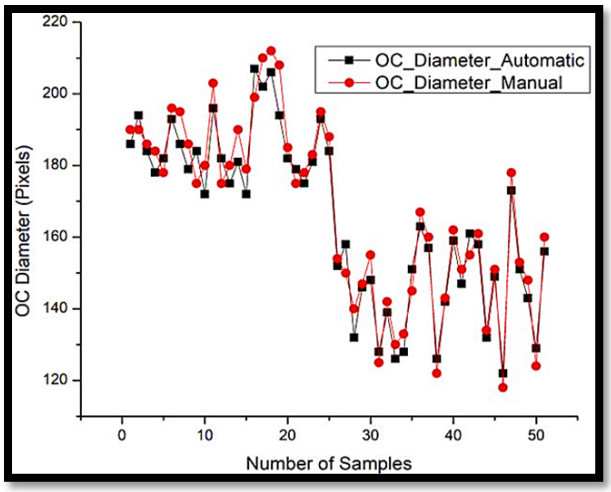

Fig. 8b: This figure represents the comparison of the diameter of the Optic Cup segmented by using manual and automated processes.

The calculation of the CDR, an essential pointer in the detection of glaucoma and hypertension, involves measuring the optic cup and optic disc areas and determining their ratio. Normal patients typically have a CDR below 0.6, while patients with

abnormalities tend to have a CDR above 0.6. Fig. 9 depicts the error comparison between the automated CDR and manual CDR, serving as an evaluation of the approach's performance. This figure illustrates the distribution of errors across 50 sample images. From the results displayed in Fig. 9, it is evident that our Active-BDCLF method achieves a maximum error for the CDR of approximately less than ±4%. Additionally, the average mean error is intended to be almost6.11%, demonstrating the higher accuracy of the CDR measurement. These findings indicate that Active-BDCLF outperforms other methods in this context.

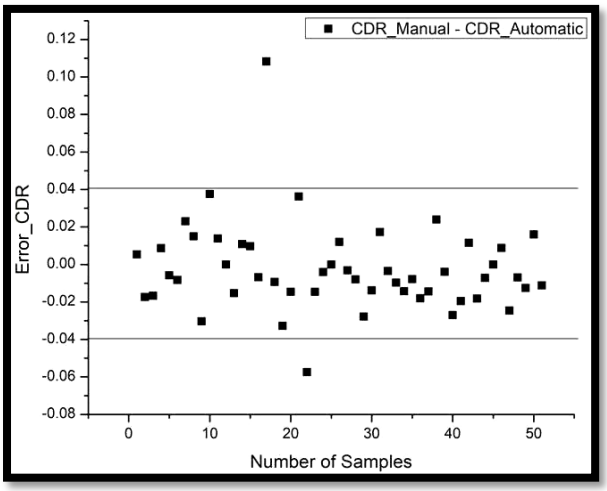

Fig. 9: The result shows the error in the Cup-Disk Ratio calculated automatically and manually.

Figure 10 is offered to gauge the effectiveness of the proposed method. It compares glaucoma detection results from our proposed method with those from the manual method. A CDR value greater than 0.60 is used to identify a patient as a potentially abnormal case. It is found that the Active-BDCLF process has average sensitivity, specificity, and precision are 95.83%, 98.23%, and 96.49%

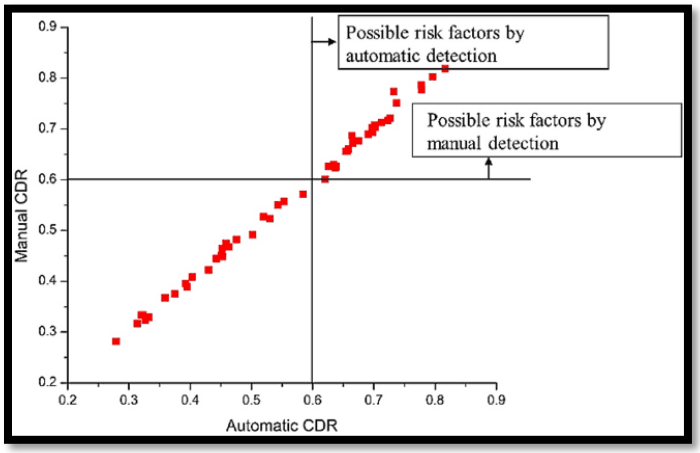

Fig. 10: This figure represents the dataset ranging from normal to possible risk factors [1].

The performance quality of various classifiers is determined by computing assessment metrics such as accuracy, specificity, and sensitivity, which are obtained using equations (23), (24), and (25).

$$Accuracy = \frac{TP+TN}{TP+TN+FP+FN} \quad (23)$$

$$Specificity = \frac{TN}{TN+FP} \quad (24)$$

$$Sensitivity = \frac{TP}{TP+FN} \quad (25)$$

Where, $TN = True\ Positive,\ TN = True\ Negative, FP = False\ Positive$ and $FN = False\ Negative$.

Table 4 presents the computation results for various metrics in the context of optical disc (OD) and optic cup (OC) analysis. Specifically, it covers sensitivity, specificity, overlapping error (OD and OC), balanced accuracy (OD and OC), and absolute error in cup-to-disc ratio (CDR), denoted asA_{OD}, A_{OC}, E_{OD}, E_{OC}, δ_E, respectively. When focusing on OD segmentation, the Active BDCLF method accomplishes a sensitivity of 98.6%, specificity of 99.7%, and accuracy of 98.5%, accompanied by an absolute error of 2.8%. Similarly, for OC segmentation, the Active BDCLF method demonstrates a sensitivity of approximately 97.7%, specificity of 98.7%, accuracy of 96.8%, and a minimum error of 2.8%. These results further establish the superiority of the PROPOSED technique over alternative methods.

Table 4: Statistical results of optic cup and optic disk

Dataset	Sensitivity		Specificity		Accuracy		E_{OD}	E_{OC}	δ_E
	OD	OC	OD	OC	OD	OC			
CHASEDB1	0.962	0.953	0.997	0.983	0.975	0.968	0.103	0.103	0.049
DRIVE	0.968	0.947	0.984	0.972	0.971	0.945	0.087	0.294	0.045
HRF	0.986	0.977	0.984	0.987	0.985	0.962	0.074	0.241	0.028
STARE	0.950	0.932	0.976	0.975	0.953	0.960	0.093	0.285	0.069

In the preceding section, wavelet terms were applied for energy minimization. However, thin vessels can sometimes be removed when their orientations differ from those of the wavelet terms. Additionally, high intensity can be exhibited by non-vessel structures, such as pathological regions. In such scenarios, edges have struggled to be accurately detected by the active contour, often resulting in the misclassification of pathological regions as vessels. For example, as shown in Fig. 11, this issue is demonstrated in a portion of an image containing signs of pathology. Here, edges are not detected effectively by the active contour, leading to the misinterpretation of pathological regions as vessels. The ability of the active contour to update the evolution function in subsequent iterations can be further hindered by high-intensity regions. Edge detection errors are often caused by factors such as the presence of pathology, intensity variations within the image, or inconsistencies in the level set function that arise during the evolution process, potentially destabilizing it.

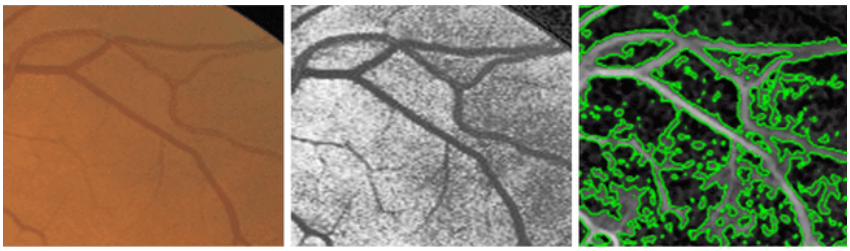

Fig. 11: Image part from DRIVE dataset (a) the input image, (b) image with applied enhancement, (c) active contour result after 100 iterations.

Therefore, a solution for modification called 'reinitialize' is used, but it is difficult to implement. 'Reinitialize' is not available in the active contour. A performance enhancement framework is used to prevent the evolutionary equilibrium from being destroyed, which strives to maintain the outline along the borders of the image. An

equation for modifying the evolution function is developed by the proposed algorithm as shown below:

$$E_{optimal}(x,y) = \alpha_1 E_n(x,y) + \alpha_2 I_{Hessian}(x,y)E_n(x,y) + \alpha_3 I_{match}(x,y)E_n(x,y)$$

Where $\alpha_1 > 0, \alpha_2 > 0, and\ \alpha_3 > 0$ are the coefficients that regulate the importance of each term. $E_n(x,y)$ can be achieved from the following equation.

$$E_n(x,y) = E_{n-1}(x,y) + \Delta t.F(\phi,x,y)$$

Where $F(\phi,x,y)$is the potential operator, Δt is the time phase, and n is the iteration frequency. E_0 is the initial curve and its obtained as $E_0(x,y) = \phi_0(x,y)\phi(0,x,y)$. $I_{Hessian}$ and I_{match} in equation 6 are Binary representations derived from the Hessian matrix [61] and matched filter [62], respectively. A matched filter is considered a framework for vessels. It is typified by a second-dimensional Gaussian filter and is merged with the main picture. The convolution matrix is utilized in various iterations. The kernel completes twelve rotations in 15° stages and adapts to differently oriented vessels. The peak performance of the filter is determined per pixel, and a boundary criterion is next utilized to supply a binary vessel structure. In [61], a vessel enhancement filter utilizing the Hessian matrix components is discussed. The Hessian is a square array that holds the second-order partial derivatives. These frameworks can be molded by the intricacies of the image and three-second derivatives $Gaussian_x x$, $Gaussian_y y$, $Gaussian_x y$ as $H(f) = \begin{bmatrix} f_{xx} & f_{xy} \\ f_{xy} & f_{yy} \end{bmatrix}$. Eigenvalues γ_1 and γ_2 are measured as $\gamma_1 = 1/2\left(f_{xx} + f_{yy} + temp\right)$ and $\gamma_2 = 1/2\left(f_{xx} + f_{yy} - temp\right)$. The $temp$ function is achieved as $temp = \sqrt{\left(\left(\mathrm{f_{xx}} - \mathrm{f_{yy}}\right)^2 + 4\mathrm{f_{xy}^2}\right)}$. The hessian filter is measured as:

$$\text{Hessian} = \begin{cases} 0 & \text{if } \gamma_2 > 0 \\ \exp\left(-\dfrac{\mathrm{R_\beta^2}}{2\beta^2}\right)\left(1 - \exp\left(-\dfrac{\mathrm{s}}{2c^2}\right)\right) & \text{otherwise} \end{cases}$$

Where $\mathrm{R_\beta} = \frac{\gamma_1}{\gamma_2}$ and $\mathrm{s} = \sqrt{\gamma_1^2 + \gamma_2^2}$. The Hessian matrix demonstrates qualities including noise removal, recognition of linear structures, and spot-like appearances.

The final step involves the extraction of the vessel tree. Different strategies for sorting are available. In this approach, basic thres holding with a global threshold criterion obtained from Otsu's method [63] was used. Two classes of pixels are present in the vessel segmentation: the pixel (i, j) is assigned to either the foreground or the background. The optimum threshold separating these classes is calculated by the Otsu algorithm, ensuring that their interclass variance is maximized [63]. The optic discs or bright lesions can increase false positives. Additionally, some thin vessels are fragmented. Therefore, post processing is required to restore fragmented edges and the eliminate of noise.

Morphological operators were used for this work. Noise pixels, which are not part of the vascular network, were eliminated by considering a threshold level based on the number of pixels, with regions having fewer pixels than the threshold being discarded. For linking edges, the bridge morphologies operator was used. The bridge operator ties pixels together that each has two nonzero neighboring pixels. The separation of the vessel of the overall image by using the proposed active contour technique is shown in Fig. 12. Fig. 12 compares the manual and automatic results of the vessel's structure with respective input images. Compared to other pre-existing techniques, this method offers superior accuracy and faster processing time. The proposed automated method for segmenting vessels attains an average accuracy of 98.4% and a sensitivity of 97.6%.

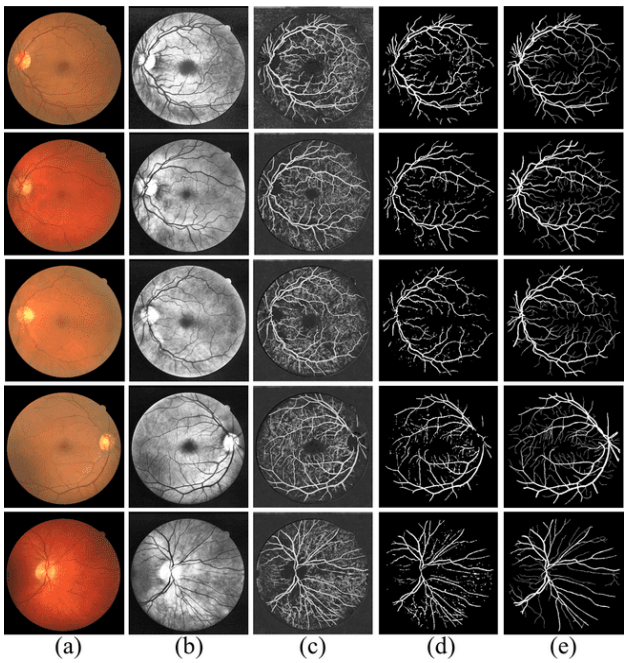

Fig. 12: Result shows the overall vessels segmentation using active contour by fusioning CLAHE and Blind Deconvolution: (a) Input RGB fundus image, (b) CLAHE and Blind Deconvolution fusion-based Enhancement, (c) Vessels after applying Active Contour function, (d) Active Contour based segmentation, (e) Manual Segmentation.

Fig. 13 explains the vessel mapping and artery-vein separation within the mentioned specific ring mask. The ring mask has been chosen for complexity due to the vessel's branching.

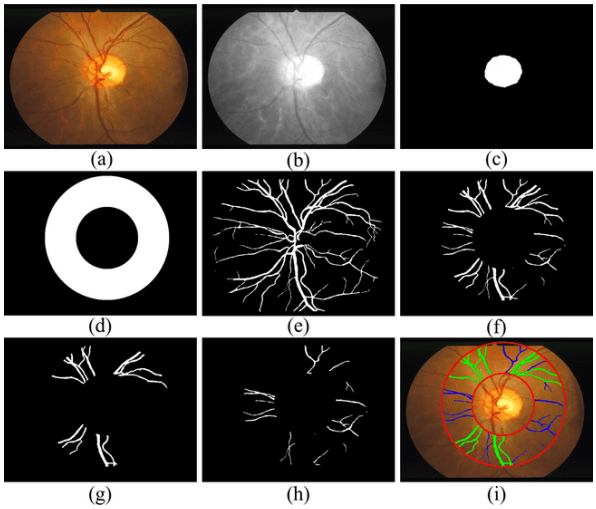

Fig. 13: Result shows the separation of arteries and veins within specified ring mask: (a) The Input RGB Image, (b) Red components of RGB image, (c) Segmented optic disk, (d) (3D-1.5D) mask, (e) Segmented Vessels (f) Segmented vessels within mask, (g) Separated veins, (h) Separated arteries, and (I) Segmented vessel's labeling.

The evaluation metrics, accuracy, and sensitivity are calculated for various classifiers to assess their qualitative performance. Table 5 presents the results of compilation the recital of the Active-BDCLF system with previously established methods. The table indicates that our proposed method outperforms the other techniques in retinal vessel segmentation, with a sensitivity ranging from 96.58% to 98.73%. Additionally, our Active-BDCLF method surpasses the conventional methods in terms of accuracy, achieving an accuracy of 98.56%.

Table 5: The results show the performance analysis of the proposed technique compared to the previously established methods.

Algorithm	Dataset	Samples	Sensitivity (%)	Specificity (%)	Accuracy (%)
Li et al [54]	DRIVE	40	75.69	98.16	95.27
	STARE	20	77.26	98.44	96.28
	CHASEBD1	28	75.07	97.93	95.81
Srinidhi et al. [55]	DRIVE	40	86.44	96.67	95.89
	STARE	20	83.25	97.46	95.02

	CHASEBD1	28	82.97	96.63	94.74
Yan et al. [56]	DRIVE	40	76.31	98.20	95.38
	STARE	20	77.35	98.57	96.38
	CHASEBD1	28	76.40	98.06	96.07
Jin et al. [57]	DRIVE	40	79.63	98.00	95.66
	STARE	20	75.95	**98.78**	96.41
	CHASEBD1	28	81.55	97.52	96.37
Yuchen Yuan et al. [58]	DRIVE	40	80.46	98.05	95.81
	STARE	20	79.14	98.70	96.65
	CHASEBD1	28	84.02	98.01	96.73
Active-BDCLF	HRF	45	**96.58**	97.65	**98.56**
	DRIVE	40	**97.23**	96.69	**97.39**
	CHASEDB1	28	**98.41**	95.31	**98.14**
	STARE	20	**98.73**	96.45	**98.37**

To measure vessel width, the center line and the edges of the first vessels are computed from the segmented binary vessels using thinning and canny edge detection methods. These images are then mapped to locate the vessel width for a pixel position on the specific vessel center line, fig. 14.

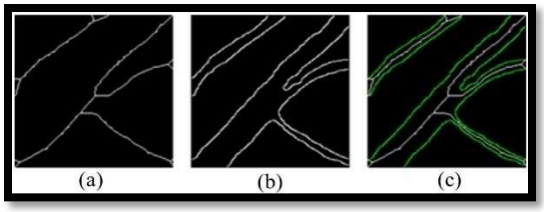

Fig.14: Results representing: (a) vessel's skeleton, (b) vessel's edge, (c) mapping of (a) and (b).

To measure the vessel's width, a pixel from its centerline image is taken into account, subsequently, a mask is applied with the center pixel at its core. This mask aims to identify the edge pixels near the centerline pixel. Every pixel location within the mask is established by advancing the pixel position incrementally until the mask's size is reached and rotating each position from 0° to 180° relative to the center pixel simultaneously. To extend the angle of rotation, the step size is considered to be less than 180° divided by the mask length.

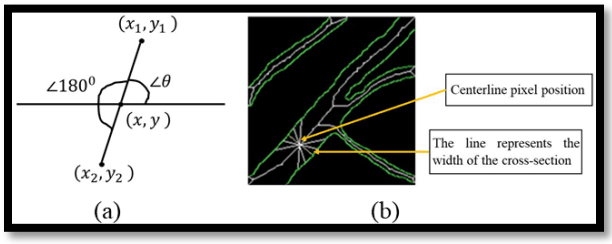

Fig. 15: This figure represents the process (a) finding the edge pixels and (b) the vessel's width or minimum distance of pair pixels.

Edge pixel intensity has been searched for each obtained position to determine whether it is border pixel or not. Once the pixel's boundary is measured, its minor is identified by shifting the angle by 180 degrees and expanding the distance from one to the mask's maximum dimension [fig. 15]. Thus, a rotationally invariant mask is created, and all possible pixel pairings are picked to find the width or diameter of that cross-sectional area.

$x_1 = x + r\cos(\theta)$ (26)

$y_1 = y + r\sin(\theta)$ (27)

Where,(x, y) is the vessel centerline pixel position, $r = 1,2,3,\ldots\ldots,$(mask size/ 2)and $\theta = 0^0,\ldots\ldots\ldots,180^0$. For any pixel position, if the binary parameter in the edge image is 1 then the pixel (x_2, y_2) in the opposite edge has been measured by considering $\theta = 180^0 + \theta$and by varyingr.

After operating, a pair of pixels was discovered on the opposite edge. The minimum Euclidean distance, $\sqrt[2]{(x_1 - x_2)^2 + (y_1 - y_2)^2}$, was calculated from this pair of pixels to determine the width of the vessel's cross-section. Table 5 displays the resulting widths at 20 distinct cross-sections of the vessel as shown in figure 15b.

Measuring the width of the vessel is crucial because it helps determine the AVR, which indicates the severity of the disease based on the condition of the retinal image. Table 6 provides a comparison of vessel widths obtained using the proposed automated technique and manual measurements. Two images from each dataset (HRF and DRIVE) were chosen for analysis.

Table 6: Result of Euclidean Width of 20 cross section of figure (14b)

Cross Sections	Centerline Pixel Position	Width-Line End Point		Vessel's Width (Euclidean Distance)
	(x, y)	(x_1, y_1)	(x_2, y_2)	
1	(17,27)	(13,69)	(20,75)	9.22
2	(45, 48)	(41,42)	(50,53)	14.21
3	(53,42)	(48,37)	(58,46)	13.45
4	(58,38)	(53,33)	(61,43)	12.80
5	(41,166)	(29,155)	(55,177)	34.06
6	(50,157)	(36,147)	(62,170)	34.71
7	(65,142)	(52,128)	(79,152)	36.12
8	(74,131)	(59,119)	(88,143)	37.64
9	(69,125)	(65,114)	(92,137)	35.47
10	(108,80)	(100,75)	(116,87)	20.00
11	(116,70)	(108,63)	(123,78)	21.21
12	(125,63)	(117,55)	(133,70)	21.93
13	(136,52)	(128,45)	(144,60)	21.93
14	(124,95)	(121,92)	(129,98)	10.00

15	(135,88)	(133,85)	(137,90)	6.40
16	(143,80)	(140,76)	(146,84)	10.00
17	(147,77)	(143,74)	(150,82)	10.63
18	(132,153)	(135,150)	(129,156)	8.48
19	(144,161)	(147,158)	(141,163)	7.81
20	(159,170)	(162,168)	(156,173)	7.81

Table 7 presents the automated measurements of retinal vessel width using Active-BDCLF, along with manually collected data. It also illustrates the automatic and manual calculations of AVR, showcasing a marginal average error of less than ±4% as shown in Figure 17. A normal retinal image is characterized by an AVR range exceeding 6.6, whereas a range below this threshold indicates abnormalities related to glaucoma or hypertension [1]. Consequently, the Active-BDCLF technique proposed in this study is capable of effectively assessing retinal data abnormalities, rendering it highly favorable.

Table 7: The outcome presents a comparison between the widths of the vessel acquired through the automated method proposed and those obtained through manual measurements.

Sl. No.	**$Width_{Auton}$**		**$Width_{Manu}$**		**AVR**		**ERROR**
	Artery	**Vein**	**Artery**	**Vein**	**Auto**	**Manual**	
1	11.75	21.40	12.20	23.40	0.549	0.521	-0.027
2	18.02	27.31	17.46	26.57	0.659	0.657	-0.002
3	17.69	38.83	17.85	40.02	0.455	0.446	-0.009
4	14.8	28.	15.6	31.1	0.525	0.502	-

	7	28	5	4			0.023
5	3.16	4.47	6.41	8.94	0.706	0.717	0.010
6	2.76	3.61	2.81	3.60	0.764	0.780	0.016
7	10.50	15.80	9.4	13.60	0.664	0.691	0.026
8	10.63	13.45	10.76	13.41	0.790	0.802	0.012
9	6.83	10.82	5.32	7.81	0.631	0.681	0.050
10	2.03	6.08	2.06	6.32	0.333	0.325	-0.007

Fig. 16 displays the assessment result of automatic and physically calculated AVR and error of the projected technique whereas fig. 17 represents the percentage of error in detection of AVR.

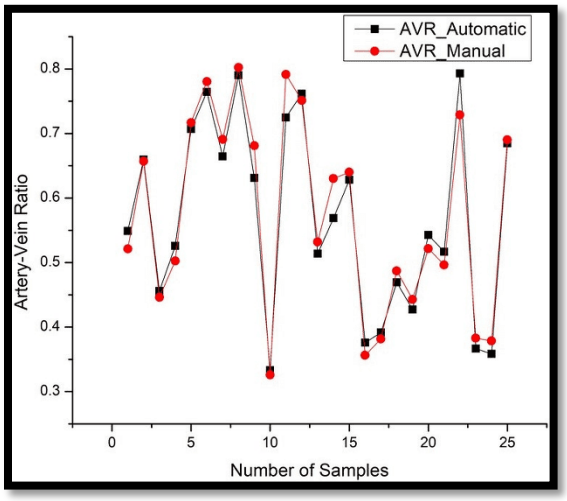

Fig.16: Results shows the comparison of automatic measured AVR with manual AVR.

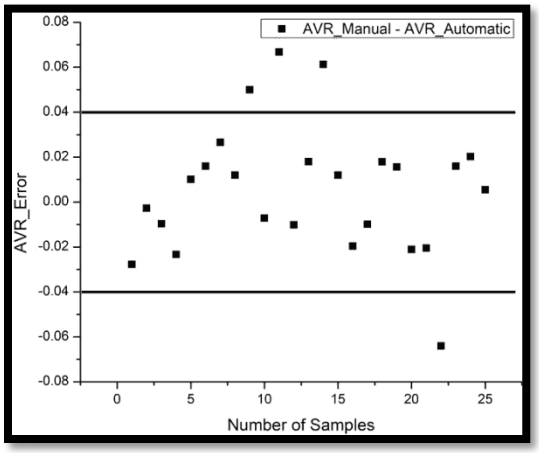

Fig 17: Result shows the percentage of error in the detection of automatic AVR

The presentation evaluation of a binary classifier system was conducted using the receiver operating characteristic (ROC) curve displayed in Fig. 18. This curve portrays the association between the true positive rate (sensitivity) and the false positive rate (1 - specificity) with varying classification thresholds. By visualizing the classifier's performance at various thresholds, the ROC curve enables the assessment of its ability to distinguish between positive and negative instances. Additionally, it facilitates the comparison of different classifiers or models. In this particular ROC curve, the dataset from the drive was utilized to analyze the performance of five distinct techniques, including the proposed Active-BDCLF method. Results indicate that the PROPOSED method outperforms existing techniques in terms of ROC, as evidenced by its faster and more stable curve. A stable ROC curve signifies that the classifier's performance remains consistent and reliable across diverse datasets or conditions, thereby instilling confidence in its generalization capability to new and unseen data. Furthermore, these findings establish the superiority of the proposed Active-BDCLF method over existing approaches.

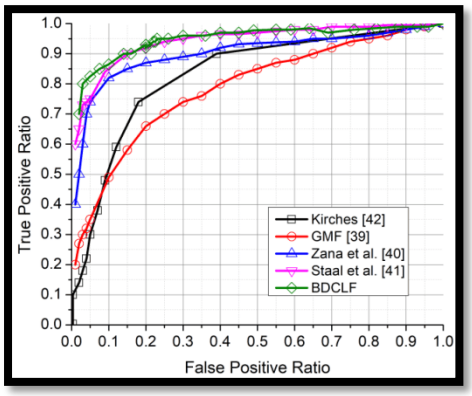

Fig.18: The average ROC plot for 40 DRIVE data is shown using five different methods.

The AVR and CDR values obtained through the Active-BDCLF method, as shown in Table 8, are applied to measure the condition of the patient in terms of diabetes, glaucoma, and overall health. To accomplish this, a selection of retinal images from the HRF dataset, encompassing diabetic, glaucoma, and healthy cases, were randomly chosen. The results obtained were promising, revealing an average CDR of 0.68 for diabetic patients, 0.62 for glaucoma patients, and 0.41 for healthy individuals. Similarly, the average AVR values were found to be 0.52 for diabetics, 0.43 for glaucoma patients, and 0.75 for those without any eye-related conditions.

Table 8: Result shows the AVR and CDR for patient's different health conditions.

HRF Image	Patent's Condition	OD (Avg.)	OC (Avg.)	W_{Artery} (Avg.)	W_{Vein} (Avg)	CDR	AVR
01_dr	Diabetic	372	294	13.15	32.37	0.63	0.41
02_dr		375	306	12.32	22.62	0.67	0.54
03_dr		327	281	14.05	23.18	0.74	0.61
04_dr		336	268	13.19	26.39	0.64	0.50
01_h	Healthy	410	248	17.39	20.81	0.37	0.84
02_h		408	267	16.18	23.41	0.43	0.69
03_h		396	237	17.02	22.11	0.36	0.77
07_h		416	278	17.36	24.79	0.45	0.70
01_g	Glaucoma	338	261	12.27	26.58	0.60	0.46
08_g		367	292	11.43	28.91	0.63	0.39

8. Conclusion:

An automated approach has been proposed to evaluate two specific target features in the human eye, namely CDR and AVR, to detect abnormalities associated with conditions like diabetes, glaucoma, and hypertension. The results obtained so far are promising, demonstrating high levels of accuracy: 98.6% for OD, 97.8% for OC, and 98.55% for AVR, with only minor errors. This technique surpasses other established methods in terms of speed due to its fully automated nature, and it requires minimal expertise for implementation, making it accessible to individuals with any level of medical knowledge. The positive outcomes achieved through this method allow for the measurement of various parameters (such as nicking, narrowing, and branching coefficients), which can assist in diagnosing different diseases.

A series of clinical images acquired from publicly available datasets will be quantitatively evaluated in the next study to find the retinopathy of prematurity (ROP).

References

1) Srinivasan Senthil Kumari, Mohan Neethu, Radhakrishnan Santhi, Subbiah Ramaswami Krishnadas, and Veerappan Muthukkaruppan, Identification of glaucomatous optic nerve head changes in Indian donor eyes without clinical history, Indian Journal of Ophthalmology, vol. 63, no. 7, pp. 600-605 (2015).
2) K. Narasimhan, V. C. Neha, K. Vijayarekha, et al., Hypertensive retinopathy diagnosis from fundus images by estimation of AVR, ICMOC – 2012, Elsevier Ltd., pp. 980 – 993 (2012).
3) Kingman S., Glaucoma is second leading cause of blindness globally, Bull World Health Organ, vol. 8 pp. 82-887 (2004).
4) George R, Ve RS, Vijaya L., Glaucoma in India: Estimated burden of disease, J Glaucoma, vol. 7, pp. 19-391 (2010).
5) T. Y. Wong, R. Klein, A. R. Sharrett, et al., Retinal arteriolar diameter and risk for hypertension, Ann. Intern. Med., vol. 140, pp. 248-255 (2004).
6) T. Y. Wong, R. Klein, F. J. Nieto, et al., Retinal microvascular abnormalities and 10-year cardiovascular mortality: a population-based case-control study, Ophthalmology, vol. 110, pp. 933-940 (2003).
7) T. Y. Wong, R. Klein, et al., Hypertensive retinopathy and risk of stroke, published online in Hypertension (2013).
8) Claudia Kondermann, Daniel Kondermann, Michelle Yan, Blood Vessel Classification into Arteries and Veins in Retinal Images, Article in Proceedings of SPIE - The International Society for Optical Engineering, (2007).
9) Pooja Chaudhari, Prof. Girish A. Kulkarni, Using Artificial Neural Network to Detect Glaucoma with the Help of Cup to Disk Ratio, International Journal of Advanced Research in Electronics and Communication Engineering, vol. 5, no. 7, pp. 1967-1972 (2016).
10) Kurnika Choudhary, ANN Glaucoma Detection using Cup-to-Disk Ratio and Neuroretinal Rim, International Journal of Computer Applications, vol. 111, no. 11, pp. 8-14 (2015).
11) Tehmina Khalil, Samina Khalid and Adeel M. Syed, Review of Machine Learning Techniques for Glaucoma Detection and Prediction, Science and Information Conference, London, UK, pp. 27-29 (2014).
12) T. Teng, M. Lefley, and D. Claremont, Progress towards automated diabetic ocular screening: A review of image analysis and intelligent systems for diabetic retinopathy, Med. Biol. Eng. Comput., vol. 40, pp. 2–13 (2002).
13) R. M. Cesar, Jr, and H. F. Jelinek, Segmentation of retinal fundus vasculature in nonmydriatic camera images using wavelets, in Angiography and Plaque Imaging,

Advanced Segmentation Techniques, J. S. Suri and S. Laxminarayan, Eds. Boca Raton, FL: CRC, pp. 193–224 (2003).

14) J. Staal, M. D. Abramoff, M. Niemeijer, M. A. Viergever, and B. van Ginneken, Ridge-based vessel segmentation in color images of the retina, IEEE Trans. Med. Imag., vol. 23, no. 4, pp. 501–509 (2004).
15) C. Heneghan, J. Flynn, M. O'Keefe, and M. Cahill, Characterization of changes in blood vessel width and tortuosity in retinopathy of prematurity using image analysis, Med. Image Anal., vol. 6, pp. 407–429 (2002).
16) A. J. Campilho, A. M. Mendonça, and J. R. Nunes, Image analysis techniques for avascular region detection in retinal angiography, in Proc. ICIAP, pp. 624–628 (1992).
17) E. Grisan and A. Ruggeri, A divide and imperial strategy for the automatic classification of retinal vessels into arteries and veins, in Proc. 25th Int. Conf. IEEE Eng. Med. Biol. Soc., pp. 890–893 (2003).
18) Y. Hatanaka, H. Fujita, M. Aoyama, H. Uchida, and T. Yamamoto, Automated analysis of the distributions and geometries of blood vessels on retinal fundus images, Proc. SPIE Med. Imag. 2004: Image Process., vol. 5370, pp. 1621–1628 (2004).
19) M. Foracchia, E. Grisan, and A. Ruggeri, Extraction and quantitative description of vessel feature hypertensive retinopathy fundus images, in Book Abstracts 2nd Int. Workshop Comput. Asst. Fundus Image Anal., pp. 6 (2001).
20) X. Goa, A. Bharath, A. Stanton, A. Hughes, N. Chapman, and S. Thom, A method of vessel tracking for vessel diameter measurement on retinal images, in Proc. ICIP, pp. 881–884 (2001).
21) M. E. Martinez-Perez, A. D. Hughes, A. V. Stanton, S. A. Thom, N. Chapman, A. A. Bharath, and K. H. Parker, Retinal vascular tree morphology: A semiautomatic quantification, IEEE Trans. Biomed. Eng., vol. 49, no. 8, pp. 912–917 (2002).
22) J. Lowell, A. Hunter, D. Steel, A. Basu, R. Ryder, and R. L. Kennedy, Measurement of retinal vessel widths from fundus images based on 2-D modeling, IEEE Trans. Med. Imag., vol. 23, no. 10, pp. 1196–1204 (2004).
23) D. E. Becker, A. Can, J. N. Turner, H. L. Tanenbaum, and B. Roysam, Image processing algorithms for retinal montage, synthesis, mapping, and real-time location determination, IEEE Trans. Biomed. Eng., vol. 45, no. 1, pp. 115–118 (1998).
24) H. Shen, B. Roysam, C. V. Stewart, J. N. Turner, and H. L. Tanenbaum, Optimal scheduling of tracing computations for real-time vascular landmark extraction from retinal fundus images, IEEE Trans. Inf. Technol. Biomed., vol. 5, no. 1, pp. 77–91 (2001).

25) Subhasis Choudhury, Shankar Chatterjee, Norman Kata,z et al. Detection of blood vessels in retinal images using two dimensional matched filter, IEEE Transactions on Medical Images, vol. 8, No. 3, pp. 264 – 269 (1987).
26) James Lowell, Andrew Hunter et al. Measurement of retinal vessels width from fundus images based on 2-D modeling, IEEE Transactions on Medical Imaging, vol. 3, No. 10, pp. 1200 – 1203 (2004).
27) Di Wu, Ming Zhang et al. Adaptive detection of blood vessels in retinal images, IEEE Transactions on Biomedical Engineering, vol. 53, No. 2, pp. 341-343 (2006).
28) Zhang, Zhuo, Beng Hai Lee, Jiang Liu, Damon Wing Kee Wong, Ngan Meng Tan, Joo Hwee Lim, Fengshou Yin, Weimin Huang, Huiqi Li, and Tien Yin Wong., Optic disc region of interest localization in fundus image for glaucoma detection in ARGALI, In 2010 5th IEEE Conference on Industrial Electronics and Applications, IEEE, pp. 1686-1689 (2010).
29) Dehghani, Amin, Hamid Abrishami Moghaddam, and Mohammad- Shahram Moin., Optic disc localization in retinal images using histogram matching, EURASIP Journal on Image and Video Processing 2012, no. 1, pp. 19 (2012).
30) Akram, M. Usman, Aftab Khan, Khalid Iqbal, and Wasi Haider Butt., Retinal images: optic disk localization and detection, In International Conference Image Analysis and Recognition, Springer, Berlin, Heidelberg, pp. 40-49 (2010).
31) M. Kirubaa, R; Dr. Lavanya R.; Nazneen P Kotwal; Devi Vijayan, change detection in mammogram images using fuzzy C-means clustering, International Journal of Applied Engineering Research 10(11):29825-29834 (2015).
32) "Inspire Datasets", University of Iowa, Carver College of Medicine, Department of Ophthalmology and Visual Science, available online at medicine.uiowa.edu.
33) "High-resolution fundus (HRF) image database" available online at www5. cs. fau. de .
34) "Structured analysis of the retina dataset" is available online at www.ces. clemson. edu .
35) Saeid F., Sevin Samadi, Parisa Nadirkhanlou, Novel Retinal Vessel Segmentation Based on Local Adaptive Histogram Equalization, 8-th Iranian Conference on Machine Vision and Image Processing (MVIP) IEEE, (2013).
36) Yitian Zhao et al., Automatic 2-D/3-D Vessel Enhancement in Multiple Modality Images Using a Weighted Symmetry Filter, IEEE Transactions on Medical Imaging, 37, (2018).
37) Ming, L., Qingbo Yin, Mingyu Lu, Retinal Blood Vessel Segmentation Based on Multi-Scale Deep Learning, Proceedings of the Federated Conference on Computer Science and Information Systems, p. 117–123 (2018).

38) Zhun, F., Yibiao, R., Jiewei, L., Jiajie, M., Fang, L., Xinye C. and Tiejun, Y, Automated Blood Vessel Segmentation in Fundus Image Based on Integral Channel Features and Random Forests, 12th World Congress on Intelligent Control and Automation (WCICA) (2016).
39) S. Chaudhuri, S. Chatterjee, N. Katz, M. Nelson, M. Goldbaum, Detection of blood vessels in retinal images using two dimensional matched filters, IEEE Trans. Med. Imaging, Vol.8(3), pp. 263-269 (1989).
40) F. Zana, J.C. Klein, Segmentation of vessel like patterns using mathematical morphology and curvature evaluation, IEEE Trans. Image Processing, Vol. 10(7), pp. 1010-1019 (2001).
41) J. Staal, B. Ginneken, M. Niemeijer, A. Viegever, M.D. Abramoff, Ridge based vessel segmentation in color images of the retina, IEEE Trans. Med. Imaging, Vol. 23(4), pp. 501-509 (2004).
42) R. Kirsch, Computer determination of the constitute structure of biomedical images, Comput. Biomed. Res. Vol. 4(3), pp. 315-328 (1971).
43) Mohammed Al-Rawi, Munib Qutaishat, Mohammed Arrar, An improved matched filter for blood vessel detection of digital retinal images, Computers in Biology and Medicine, Vol. 37, pp. 262-267 (2007).
44) Nassrallah Faris, Abdukader Al Shalchi, & Javad Rahebi, Human retinal optic disc detection with grasshopper optimization algorithm, Multimedia Tools and Applications, Springer, volume 81, pages24937–24955 (2022)
45) Buket Toptaş, Murat Toptaş & Davut Hanbay, Detection of Optic Disc Localization from Retinal Fundus Image Using Optimized Color Space, Journal of Digital Imaging, Springer, 35, pages302–319 (2022).
46) Mahum R Rehman, S Okon, OAlabrah, AMeraj, TRauf H, A novel hybrid approach based on deep cnn to detect glaucoma using fundus imaging, Electronics (Switzerland) (2022).
47) Nazir TIrtaza, AStarovoitov V, Optic Disc and Optic Cup Segmentation for Glaucoma Detection from Blur Retinal Images Using Improved Mask-RCNN, International Journal of Optics (2021).
48) Deng I, Wang Y Han J, Optical Disc Location Based on Similarity to Improved Harris Algorithm, Chinese Control Conference, CCC (2021) 2021-July 2185-2189
49) Rehman AHarouni, MKarimi, MSaba, TBahaj, & S Awan, Microscopic retinal blood vessels detection and segmentation using support vector machine and K-nearest neighbors, Microscopy Research and Technique (2022) 85(5) 1899-1914.

50) Arsalan M Haider, A Choi, J Park K, Diabetic and hypertensive retinopathy screening in fundus images using artificially intelligent shallow architectures, Journal of Personalized Medicine (2022) 12(1).
51) Pal M, Banerjee M, Retinal vessel segmentation using a strip wise classification approach with grid search-based parameter selection, International Journal of Computational Vision and Robotics (2022) 12(2) 194-218.
52) Boudegga, HElloumi, Y Akil, M Hedi, Bedoui, M Kachouri, R Abdallah A, Fast and efficient retinal blood vessel segmentation method based on deep learning network, Computerized Medical Imaging and Graphics (2021) 90.
53) Ooi, A Embong, Z Abd, Hamid A Zainon, R Wang, S Ng, T Hamzah, R Teoh, S Ibrahim H, Interactive blood vessel segmentation from retinal fundus image based on canny edge detector, Sensors, MDPI, (2021) 21(19).
54) Q. Li, B. Feng, L. Xie, P. Liang, H. Zhang, and T. Wang, A crossmodality learning approach for vessel segmentation in retinal images, IEEE transactions on medical imaging, vol. 35, no. 1, pp. 109–118, 2015.
55) C. L. Srinidhi, P. Aparna, and J. Rajan, A visual attention guided unsupervised feature learning for robust vessel delineation in retinal images, Biomedical Signal Processing and Control, vol. 44, pp. 110–126, 2018.
56) Yan, Zengqiang and Yang, Xin and Cheng, Kwang-Ting, A three-stage deep learning model for accurate retinal vessel segmentation, IEEE journal of biomedical and health informatics, vol. 23, no. 4, pp. 1427–1436, 2018.
57) Q. Jin, Z. Meng, T. D. Pham, Q. Chen, L. Wei, and R. Su, Dunet: A deformable network for retinal vessel segmentation, Knowledge-Based Systems, vol. 178, pp. 149–162, 2019.
58) Yuchen Yuan, Lei Zhang, Lituan Wang, and Haiying Huang, Multi-level Attention Network for Retinal Vessel Segmentation, ieee journal of biomedical and health informatics.
59) Kass, M., Witkin, A., Terzopoulos, D.: 'Snakes: active contour models', Int. J. Comput. Vis., 1988, 1, (4), pp. 321–331.
60) Xu, C., Prince, J.L.: 'Gradient vector flow: a new external force for snakes'. Proc., 1997 IEEE Computer Society Conf. Computer Vision and Pattern Recognition, San Juan, Puerto Rico, 1997, pp. 66–71.
61) Modava, M., Akbarizadeh, G.: 'Coastline extraction from SAR images using spatial fuzzy clustering and the active contour method', Int. J. Remote Sens., 2017, 38, (2), pp. 355–370.

62) Fraz, M.M., Remagnino, P., Hoppe, A., et al.: 'Blood vessel segmentation methodologies in retinal images – A survey', Comput. Methods Programs Biomed., 2012, 108, (1), pp. 407–433.
63) Modava, M., Akbarizadeh, G.: 'Coastline extraction from SAR images using spatial fuzzy clustering and the active contour method', Int. J. Remote Sens., 2017, 38, (2), pp. 355–370.